Military Technical College

Kobry El-Kobbah,

Cairo, Egypt

11th International Conference on Civil and Architecture Engineering

ICCAE-11-2016

Assessment of concrete-to-steel bond behaviour of reinforced concrete structures using acoustic emission intensity analysis

- Ahmed A. Abouhussien, M.A.Sc., PhD Candidate
- Department of Civil Engineering, Faculty of Engineering and Applied Science, Memorial University of Newfoundland, St. John's, Newfoundland, Canada, E-mail: aabouhussien@mun.ca, Phone: +17093306934
- Assem A.A. Hassan, Ph.D., M.A.Sc., M.Sc., P.Eng., Associate Professor
- Department of Civil Engineering, Faculty of Engineering and Applied Science, Memorial University of Newfoundland, St. John's, Newfoundland, Canada, E-mail: ahassan@mun.ca, Phone: +17098647473

Abstract. An experimental study was performed to utilize acoustic emission (AE) intensity analysis for the assessment of the concrete-to-steel bond behaviour of reinforced concrete structures. A total of 18 reinforced concrete unconfined prism samples were tested in a direct pullout test setup under incrementally increasing monotonic loading as being constantly monitored with attached AE sensors. The samples were cast using variable bar diameter (10, 20, 35 mm) and bar embedded length (50, 100, 200 mm). Different AE signals parameters were recorded throughout the tests until failure including rise time, counts, number of hits, signal strength, energy, amplitude, duration, and frequency values. Moreover, an AE intensity analysis

was applied on AE signal strength results to produce two additional AE parameters: historic index (*H (t)*) and severity (S_r). Results demonstrated that cumulative signal strength (CSS) correlated well with different degrees of loss of bond from micro-cracking till bond splitting failure, which resulted in cover cracking or delamination. The review of CSS, *H (t)*, and S_r curves allowed the detection of two progressive stages of bond deterioration (micro-cracking and macro-cracking) in all tested specimens. Intensity analysis parameters (*H (t)* and S_r) were employed to create bond damage classification chart to evaluate the concrete-to-steel bond condition in reinforced concrete structures.

Keywords: Structural health monitoring; reinforced concrete structures; acoustic emission; intensity analysis; bond behaviour; bond splitting failure.

1. Introduction

Reinforced concrete (RC) structures are designed and constructed to ensure that a perfect bond between concrete and steel is maintained throughout its service lifetime. This bond allows the transfer of longitudinal forces from steel to concrete and ensures the composite action within RC elements (ACI Committee 408, 2003; Nilson et al., 2004). The concrete-to-steel bond strength depends on a number of parameters including material and structural factors. In addition, different requirements are specified in building codes in order to design concrete structures that avoid bond failures. However, the performance of this bond may be affected when RC structures are exposed to excessive repeated loading and/or severe environmental conditions.

Structural health monitoring (SHM) systems can be applied for the real-time evaluation and assessment of different damage mechanisms in different civil structures. SHM systems can be employed for the purpose of prognosis and diagnosis of damage in concrete structures. One important application of SHM systems is the detection of bond deterioration between steel bars and concrete (Zhu et al., 2013; Ho et al., 2015). For example, Zhu et al. (2013) detected the de-bond damage between steel and concrete by means of embedded piezoelectric sensors and actuators. The results of their investigation were then used to develop three indices to evaluate the bond loss. This technique, however, is considered an active SHM system that requires an external source for generating signals to be detected by sensors. Another technique deployed fiber Bragg grating-based strain sensors to characterize bond slip in prestressed concrete bridge girders (Ho et al., 2015). This technique evaluated the local strain developed at different stages of bond slip until failure.

Acoustic emission (AE) sensors can be integrated in passive SHM systems for the prediction and characterization of various damage mechanisms in concrete structures. AE sensors have the advantage of continuous acquisition of signals released due to local damage in materials under stress (Pollock, 1986; Grosse et al., 2003; Ziehl, 2008; Nair and Cai, 2010). This technique was adopted in the literature and allowed the detection and identification of a wide variety of deteriorations in reinforced and prestressed concrete structures (Nair and Cai, 2010). A limited number of studies have investigated the application of AE monitoring for the concrete-to-steel bond of concrete structures. Iwaki et al. (2003) applied AE monitoring in reinforced concrete under pull-out tests to investigate the influence of concrete compaction on the bond behaviour of reinforced concrete elements. The results indicated the feasibility of analyzing AE activity (in

terms of cumulative number of hits) to detect the locations of insufficient bond and slippage of steel bars.

More recently, the bond behaviour of black and galvanized deformed steel in concrete subjected to pull-out tests was evaluated using AE monitoring (Gallego et al., 2015). The analysis of AE activities (cumulative number of hits) reflected different stages of bond degradation and differentiated between the behaviour of different types of steel (Gallego et al., 2015). Further research is required to implement the AE intensity analysis of signal strength for the quantification of bond deterioration in concrete structures. The purpose of this paper is to analyze the AE signal strength data collected from pull-out tests in order to identify early stages of bond degradation. The paper is also intended to employ the AE intensity analysis for quantifying the bond deterioration of unconfined reinforced concrete.

2. Experimental Setup

2.1. Mixture Proportions and Materials Properties

Reinforced concrete prism samples were cast using a normal-strength concrete mixture. The concrete mixture contained type GU Canadian Portland cement, similar to ASTM Type I (ASTM, 2012a), with a specific gravity of 3.15. In addition, natural sand and 10 mm maximum size stone were included in the concrete mixture as fine and coarse aggregates, respectively. The fine and coarse aggregates both have a specific gravity of 2.60 and water absorption of 1%. The characteristic compressive strength of the concrete mixture was determined at 28 days as per ASTM C39 (ASTM, 2012b). Moreover, the splitting tensile strength of concrete was obtained according to ASTM C496 (ASTM, 2011). Deformed carbon steel bars with variable diameters

(10mm, 20 mm, and 35 mm) were utilized as reinforcement in the concrete prism samples. These reinforcing steel bars had an average yield stress of 480 MPa and an average tensile strength of 725 MPa. The mixture properties, compressive strength, and splitting tensile strength results of the concrete mixture used in this paper are presented in **Table 1**.

Table 1 Mixture proportions and 28-day strength of the concrete mixture

Cement (kg/m^3)	10 mm stone (kg/m^3)	Sand (kg/m^3)	Water (kg/m^3)	28-day compressive strength (MPa)	28-day splitting tensile strength (MPa)
350	1168.27	778.84	140	f_c = 40.38	f_{ct} = 3.79

2.2. Description of the Tested Samples

The tested samples in this investigation were small-scale prism-reinforced concrete samples with variable dimensions. Each prism sample contained a reinforcing steel bar partially embedded in the sample with two protruding parts to allow the pull-out testing and the measurement of bar slip (**Fig. 1**). Three diameters of the reinforcing bars were used in the samples: 10 mm (10M), 20 mm (20M), and 35 mm (35M) bars. The prism samples were cast with constant concrete cover (30 mm) around the embedded steel bar. The clear concrete cover was maintained constant around the steel bar on all sides of each sample. On the other hand, the embedded length of all bars was changed as follows: 50 mm, 100 mm, and 200 mm. All samples had two PVC pipe bond breakers placed before and after the bonded length. The variable embedded length was achieved by increasing the length of the PVC pipes acting as the bond breaker from one end. The dimensions of the prisms were varied based on bar diameter. Two identical samples were prepared from each specimen to act as a replicate to verify the repeatability of the test result. The

detailed dimensions of all tested prism samples are tabulated in **Table 2**. After mixing, concrete was poured in wooden formwork with the reinforcing bars in a horizontal casting position. Sufficient compaction of all formwork was achieved by using mechanical vibration. After 24 hours of mixing, the specimens were de-molded and then water-cured for a period of 28 days before pull-out testing. The tested samples were designated based on the bar diameter (10M, 20M, 35M), embedded length (A for 50 mm, B for 100 mm, C for 200 mm), and replicate number (1, 2). For example, the first duplicate of the prism sample cast with 10M bar with embedded length of 100 mm is designated as 10M30B-1.

Table 2 Test matrix and specimen dimensions

Sample number	Sample designation	Bar diameter (mm)	Cover thickness (mm)	Embedded length (mm)	Dimensions (mm x mm x mm)
1	10M30A-1	10	30	50	70 x 70 x 260
2	10M30A-2	10	30	50	70 x 70 x 260
3	10M30B-1	10	30	100	70 x 70 x 260
4	10M30B-2	10	30	100	70 x 70 x 260
5	10M30C-1	10	30	200	70 x 70 x 260
6	10M30C-2	10	30	200	70 x 70 x 260
7	20M30A-1	20	30	50	80 x 80 x 260
8	20M30A-2	20	30	50	80 x 80 x 260
9	20M30B-1	20	30	100	80 x 80 x 260
10	20M30B-2	20	30	100	80 x 80 x 260
11	20M30C-1	20	30	200	80 x 80 x 260
12	20M30C-2	20	30	200	80 x 80 x 260
13	35M30A-1	35	30	50	95 x 95 x 260
14	35M30A-2	35	30	50	95 x 95 x 260
15	35M30B-1	35	30	100	95 x 95 x 260
16	35M30B-2	35	30	100	95 x 95 x 260
17	35M30C-1	35	30	200	95 x 95 x 260
18	35M30C-2	35	30	200	95 x 95 x 260

2.3. Pull-out Tests Setup and AE Monitoring Procedure

The samples were subjected to direct pull-out tests using a universal testing machine (UTM), as shown in **Fig. 1**. All samples were tested under incrementally increasing monotonic loading condition until failure. The amount of loading in each sample was recorded by means of a data-acquisition system. **Fig. 1** shows that each sample was monitored during the pull-out test using two piezoelectric AE sensors with integral preamplifier (R6I-AST) (Physical Acoustics, 2005). These sensors were mounted at one side of each sample's surface at the centre of the embedded steel bar using a two-part epoxy adhesive. The resulting acoustic emissions were continuously acquired and collected using a 4-channel AE data acquisition system and AEwin signal processing software (Mistras Group, 2007). The amplitude threshold value was assumed as 40 dB to acquire the emitted AE signals throughout the test period. The data acquisition system was setup to collect a variety of AE signal parameters including amplitude, energy, duration, signal strength, absolute energy, rise time, counts, average frequency, and peak frequency. The definitions of these parameters, along with other AE terminology used for nondestructive testing, are presented elsewhere (ASTM, 2014).

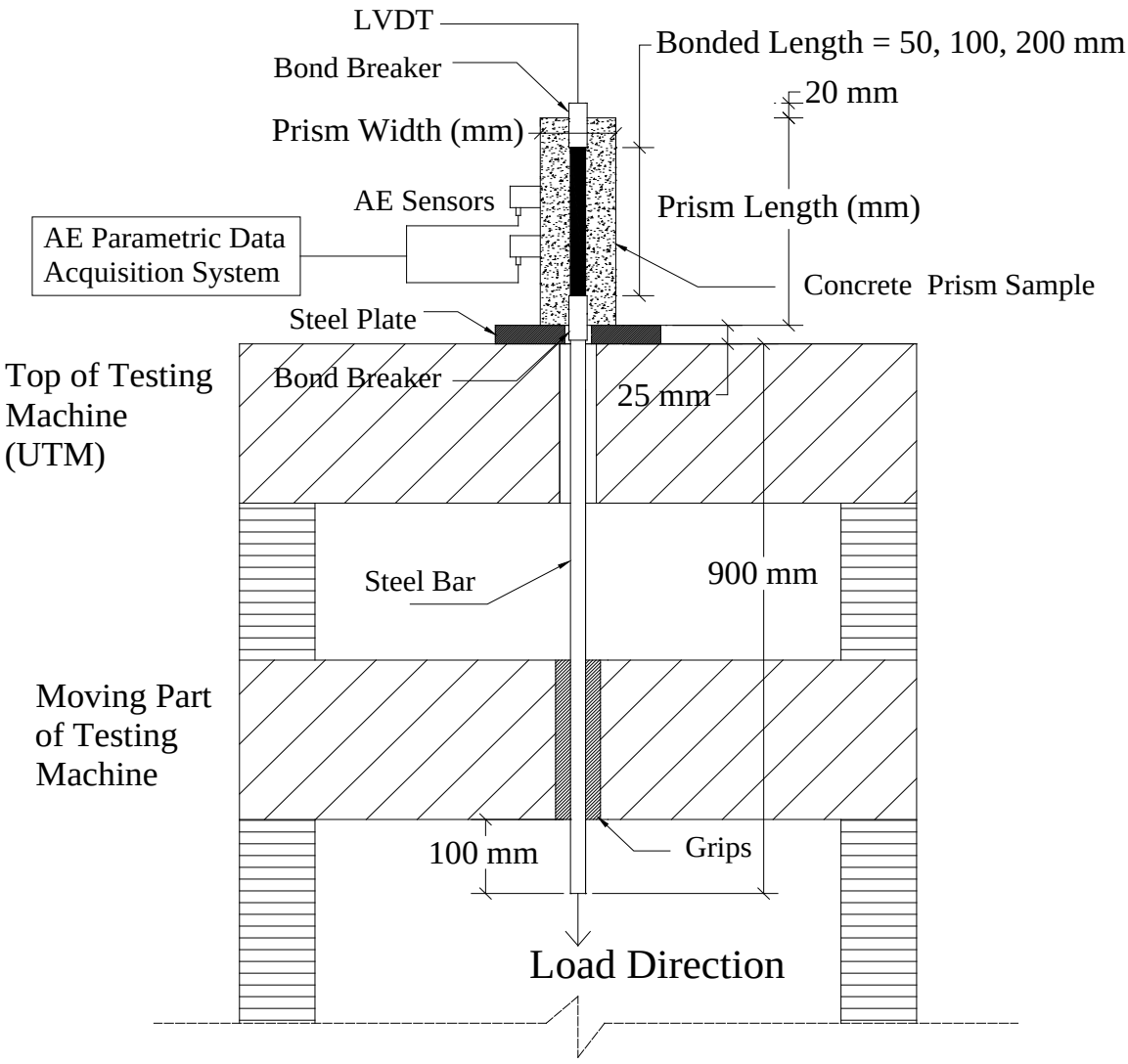

Fig. 1 Pull-out test and AE monitoring setup

3. Results and Discussions

Table 3 summarizes the results obtained from the pull-out tests performed on all tested samples. These results consist of the mode of failure, maximum load, bond strength (bond stress at the maximum recorded load), and both the load and stress at the onset of micro-cracking detected using AE analysis, as will be explained in **Section 4.3**. The results presented in **Table 3** will be compared to the results acquired from AE monitoring to evaluate the bond behaviour in all tested

samples. It is obvious from **Table 3** that most samples failed by bond splitting failure, which resulted in either splitting cracks along the bonded length at all four faces of the specimen or completely breaking the sample. For instance, the typical splitting failure of sample 20M30B-1 is shown in **Fig. 2**. On the other hand, fewer samples exhibited bar yield before any damage at the steel-concrete interface had occurred. For the purpose of evaluating the AE activities in subsequent discussions, those samples with yielded bars were utilized as a benchmark to other tested samples that failed by splitting cracking.

Table 3 Results of pull-out tests for all tested samples

Sample number	Sample designation	Failure mode	Maximum load (kN)	Bond strength (MPa)	Micro-cracking load (kN) *	Micro-cracking stress (MPa) *
1	10M30A-1	Splitting cracks	23	14.65	15	9.55
2	10M30A-2	Splitting cracks	24	15.29	14	8.92
3	10M30B-1	Bar yield	45	NA	NA	NA
4	10M30B-2	Bar yield	52	NA	NA	NA
5	10M30C-1	Bar yield	46	NA	NA	NA
6	10M30C-2	Bar yield	40	NA	NA	NA
7	20M30A-1	Splitting cracks	35	11.15	15	4.78
8	20M30A-2	Splitting cracks	39	12.42	17	5.41
9	20M30B-1	Splitting cracks	57	9.08	37	5.89
10	20M30B-2	Splitting cracks	58	9.24	49	7.80
11	20M30C-1	Broken	77	6.13	52	4.14
12	20M30C-2	Broken	103	8.20	48	3.82
13	35M30A-1	Splitting cracks	51	9.28	36	6.55
14	35M30A-2	Splitting cracks	48	8.74	23	4.19
15	35M30B-1	Splitting cracks	88	8.01	51	4.64
16	35M30B-2	Splitting cracks	74	6.73	45	4.09
17	35M30C-1	Broken	87	3.96	68	3.09
18	35M30C-2	Broken	90	4.09	76	3.46

* Detected at the beginning of micro-cracking using AE analysis

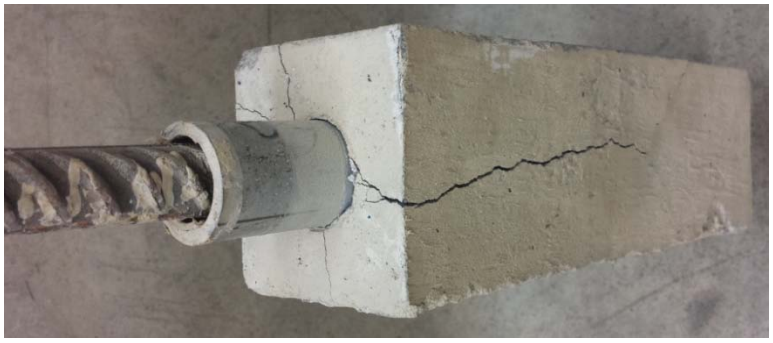

Fig. 2 Typical bond splitting cracks at failure (example sample: 20M30B-1)

3.1. AE Data Filtering

The acquired AE data collected throughout all tests were filtered to minimize any noise-related signals and/or irrelevant wave reflections within the samples' boundaries. Consequently, an amplitude-duration-based filter, or Swansong II filter, was implemented on the raw AE results obtained from all samples (Fowler et al., 1989). This filtering technique has effectively been executed in similar experimental studies dealing with AE monitoring in concrete structures (Abdelrahman et al., 2014, 2015; ElBatanouny et al., 2014; Vélez et al., 2015). This filtering technique is based on the fact that real AE signals with high amplitudes are associated with long durations, and vice versa (Abdelrahman et al., 2015). On this basis, the range of rejection limits were determined by visual inspection of all AE hits, as described in **Table 4**. All remaining AE signals in all tested samples were then deemed genuine emissions resulting from bond response. These filtered data were subsequently subjected to further analysis and will be discussed in the next section.

Table 4 Rejection limits for amplitude-duration filter

Amplitude range (dB)	Duration (μs)		Amplitude range (dB)	Duration (μs)	
	Lower	Upper		Lower	Upper
$40 \leq A < 45$	0	400	$60 \leq A < 65$	300	1000
$45 \leq A < 48$	0	500	$65 \leq A < 70$	500	2000
$48 \leq A < 52$	0	600	$70 \leq A < 80$	1000	4000
$52 \leq A < 56$	0	700	$80 \leq A < 90$	2000	7000
$56 \leq A < 60$	100	800	$90 \leq A < 100$	3000	10000

3.2. AE Intensity Analysis

Analyzing different AE signal parameters allows researchers to identify different forms of damage resulting from the deterioration of concrete structures. AE intensity analysis is a type of analysis that can be further performed on AE signal strength of the acquired AE waves to attain additional parameters to represent the severity of damage. These additional parameters can be employed to produce intensity classification charts according to the collected AE signal strength. This aforementioned analysis was first implemented in fibre-reinforced polymer (FRP) vessels (Fowler et al., 1989) and has also been extended for damage assessment in concrete structures (Rizzo et al., 2010; Abdelrahman et al., 2015; Mangual et al., 2013a, 2013b; ElBatanouny et al., 2014; Vélez et al., 2015). The AE signal strength data obtained from the current study were subjected to an intensity analysis to evaluate the bond behaviour of all tested specimens. This analysis exploited the signal strength values of all collected signals to obtain two additional AE parameters: historic index ($H(t)$) and severity (S_r). $H(t)$ represents any sudden variation in the slope of the cumulative signal strength (CSS) curve with respect to time. The magnitude of $H(t)$ in all tested samples was determined throughout the test period according to **Eq. 1** (Nair and Cai, 2010; Abdelrahman et al., 2015; ElBatanouny et al., 2014).

$$H(t) = \frac{N}{N-K} \frac{\sum_{i=K+1}^{N} S_{oi}}{\sum_{i=1}^{N} S_{oi}} \quad (1)$$

Where: N = the cumulative number of hits up to time *(t)*; and S_{oi} = signal strength of the ith event. On the other hand, S_r represents the average signal strength of the J hits having the maximum algebraic value of signal strength and calculated using **Eq. 2** (Nair and Cai, 2010; Abdelrahman et al., 2015; ElBatanouny et al., 2014).

$$S_r = \sum_{i=1}^{J} \frac{S_{oi}}{J} \quad (2)$$

The values of the constants K in **Eq. 1** and J in **Eq. 2** depend on the damage mechanism and type of structure (Vélez et al., 2015). The magnitude of K was taken based on the cumulative number of hits, as follows: a) N/A: if $N \leq 50$, b) $K = N - 30$: if $51 \leq N \leq 200$, c) $K = 0.85N$: if $201 \leq N \leq 500$, and d) $K = N - 75$: if $N \geq 501$. Conversely, J was selected as a constant value of 50, regardless of the cumulative number of hits (Nair and Cai, 2010; Abdelrahman et al., 2015; ElBatanouny et al., 2014). By substituting in **Eq. 1** and **2**, the values of both *H (t)* and S_r were obtained for all tested samples at all test intervals.

3.3. Detection of Micro-cracking and Macro-cracking Using AE Analysis

The analysis of different AE parameters has been exploited to indicate the damage in concrete structures. Among these parameters, it was found that the analysis of signal strength parameters can better represent the progression of diverse damage mechanisms in reinforced concrete structures (Nair and Cai, 2010; Rizzo et al., 2010). **Fig. 3** compares the CSS and *H (t)* results for two selected samples: sample 20M30B-1 represents samples that failed by typical bond splitting failure, and sample 10M30B-2 represents bar yielded samples associated with no damage at the

steel-concrete interface. It can be seen from **Fig. 3a** that sample 10M30B-2's CSS curve followed an almost linear increasing trend corresponding to the increase in loading until the bar yielded. Since no splitting failure occurred in sample 10M30B-2, the increase in CSS of this sample may be attributed to the transfer of force between steel and concrete by means of chemical adhesion before the occurrence of micro-cracking. In contrast, **Fig. 3c** indicates that the slope of the CSS curve witnessed two noticeable changes at nearly 220 s and 260 s from the beginning of the test. The first slope change in sample 20M30B-1 was detected at a stress value of 5.89 MPa (**Table 3**). This stress value corresponds to approximately 1.55 f_{ct}, which lies in the range of 0.8–3.0 f_{ct}. This range has already been identified in the literature as the range of stresses associated with micro-cracking initiation at the steel-concrete interface, which is followed by the onset of bar slip and macro-cracking (CEB-FIP, 2000; Gallego et al., 2015).

After the first slope change of sample 20M30B-1, the CSS curve continued to increase due to further micro-cracking and growth of macro-cracking. The second slope change of the CSS curve, with further increase of loading, can be related to the formation of macro-cracking (splitting cracks) as a result of the expected wedging action in small concrete cover thicknesses. The CSS curve also exhibited a slight rise after the second slope change until failure. This short rise in the CSS curve may be related to the increasing bar slippage values as well as widening of the splitting cracks until failure, which resulted in continuous AE activity. It should be noted that the locations of slope change in the CSS curve have been previously applied in detecting and assessing different damage mechanisms in concrete structures (Mangual et al., 2013a, 2013b; ElBatanouny et al., 2014; Abdelrahman et al., 2015; Vélez et al., 2015).

The initiation of micro-cracking and macro-cracking stages was likewise distinguished by analyzing the *H (t)* curves in **Fig. 3b**, **3d**, which show that the values of *H (t)* fluctuated throughout the test period of sample 10M30B-2 with no major variations (0.6–1.3). Conversely, as shown in **Fig. 3d**, *H (t)* showed significant changes in the other sample (20M30B-1). The first sudden increase in the values of *H (t)* for sample 20M30B-1 can be observed around 220 s (at the location of slope change in the CSS curve) with a value of 1.7. After this point, the values of *H (t)* continued to increase owing to the splitting cracks growth until reaching a maximum value of 6.05 at nearly 260 s. This maximum value also matched the point of the second slope change of the CSS curve (macro-cracking) a little before sample 20M30B-1 underwent splitting failure. On the other hand, the variations in the curves of cumulative number of hits and S_r were found to be very similar to those observed in the CSS; therefore, only the CSS and *H (t)* curves were included in **Fig. 3**. On this basis, the stage of micro-cracking in all tested samples (except those ones with bar yield) was identified and the corresponding magnitudes of load and stress are reported in **Table 3**. In addition, **Table 5** shows the AE parameter values—i.e., cumulative number of hits, CSS, *H (t)*, and S_r—at both the micro-cracking and macro-cracking stages for all tested samples.

The AE waveform parameters detected prior to micro-cracking and macro-cracking were characterized by relatively low amplitude signals (average of 50 dB). Whilst, higher amplitude signals (average of 75 dB) were associated with the detection of both micro- and macro-cracking, with no clear differences observed between the amplitudes of these signals. Thus, the analysis of the amplitude values of the collected AE waves may be used for detecting the damage, but is not a feasible method for identifying different levels of bond damage. This was

due to the non-significant changes of the amplitudes of the signals detected at both micro- and macro-cracking for all tested samples. It should be mentioned that all other AE signal parameters (duration, energy, rise time, average frequency, counts, and peak frequency) also showed non-significant variations between tested samples acquired both at micro-cracking initiation and macro-cracking. Therefore, only the cumulative number of hits, CSS, *H (t)*, and S_r parameters (**Table 5**) were considered in evaluating the effects of bar diameter, bonded length, and cover thickness on the bond behaviour.

(a)

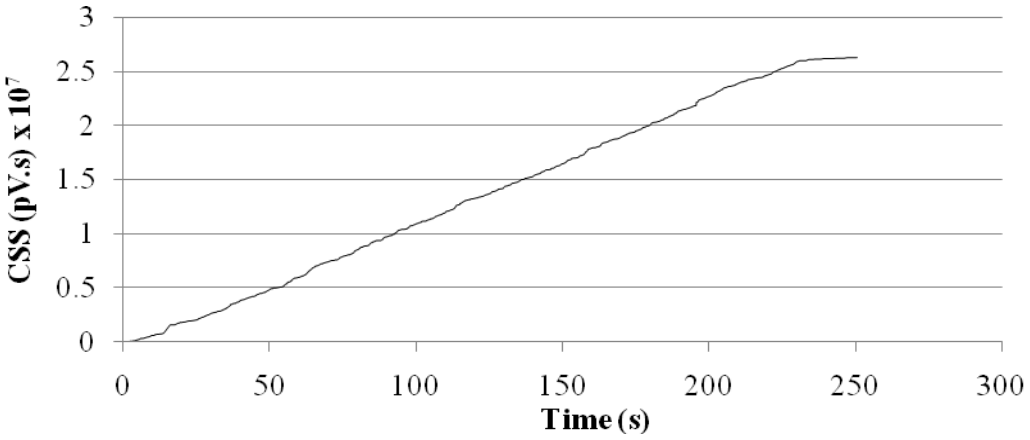

(b)

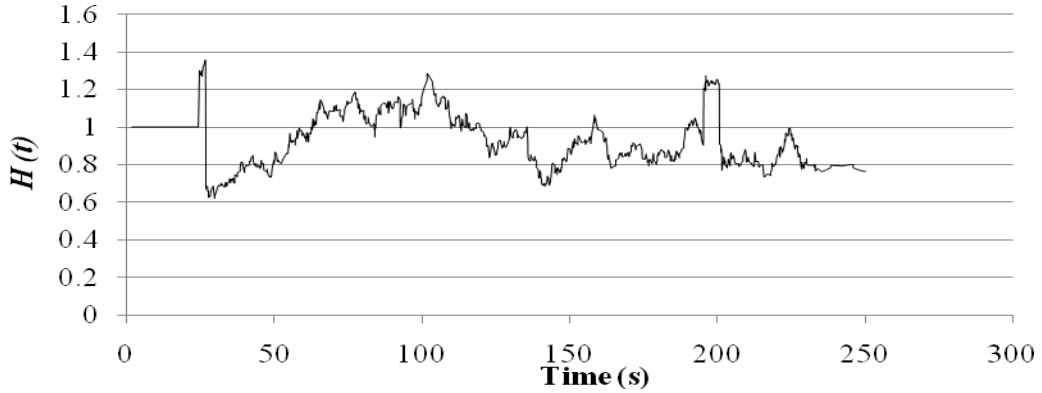

(c)

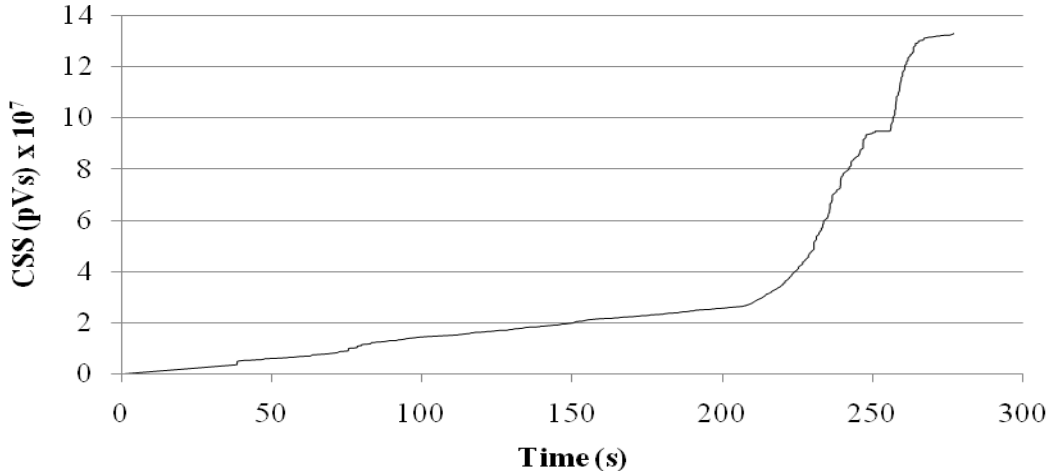

(d)

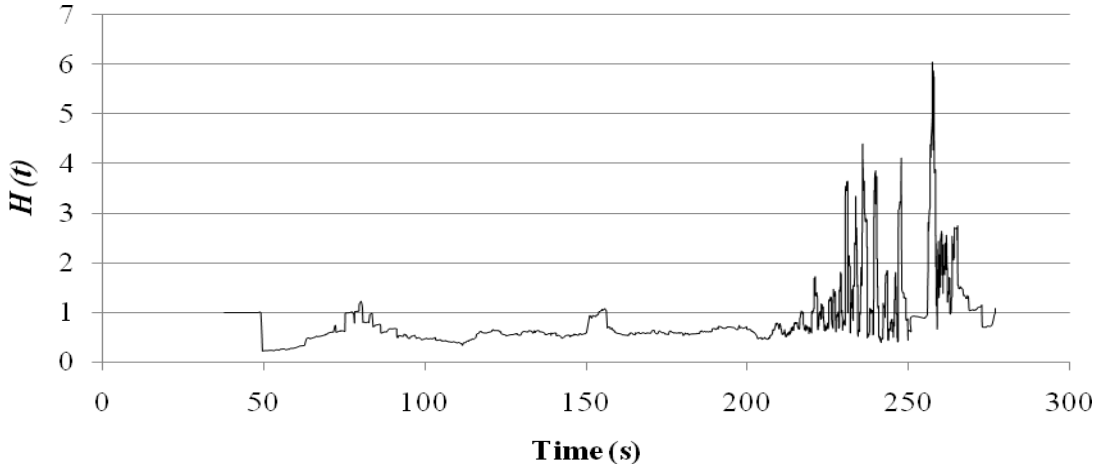

Fig. 3 CSS and *H (t)* curves: a) CSS versus test time for sample 10M30B-2, b) *H (t)* versus test time for sample 10M30B-2, c) CSS versus test time for sample 20M30B-1, and d) *H (t)* versus test time for sample 20M30B-1

Table 5 Different AE parameters detected at micro-cracking and macro-cracking

Sample	Sample designation	Cumulative number of hits				CSS (pV.s) x 10^6				*H (t)*				S_r (pV.s) x 10^4			
		Micro-cracking		Macro-cracking		Micro-cracking		Macro-cracking		Micro-cracking		Macro-cracking		Micro-cracking		Macro-cracking	
		CH1	CH2	CH1	CH2	CH1	CH2	CH1	CH2	CH1	CH2	CH1	CH2	CH1	CH2	CH1	CH2
1	10M30A-1	299	288	620	750	13.62	10.62	23.39	16.16	1.72	1.99	2.21	2.32	5.52	6.27	19.34	9.05
2	10M30A-2	318	387	546	570	9.86	14.75	15.04	17.30	1.86	2.16	3.47	3.09	8.35	6.43	17.09	17.98

3	10M30B-1	NA	NA	1839	1977	NA	NA	56.17	56.00	NA	NA	0.81	0.92	NA	NA	23.33	18.28
4	10M30B-2	NA	NA	590	1042	NA	NA	23.95	26.10	NA	NA	0.86	0.77	NA	NA	24.61	29.19
5	10M30C-1	NA	NA	2014	2788	NA	NA	77.13	89.15	NA	NA	0.88	0.79	NA	NA	33.13	37.13
6	10M30C-2	NA	NA	3236	2197	NA	NA	93.54	78.70	NA	NA	0.76	0.92	NA	NA	47.19	41.00
7	20M30A-1	542	549	836	688	11.69	12.28	94.88	90.87	2.05	2.19	3.65	3.49	10.66	12.05	56.47	39.83
8	20M30A-2	466	521	730	1013	16.96	14.97	98.19	102.37	1.90	1.59	3.16	2.85	8.74	6.73	22.98	20.80
9	20M30B-1	1019	1104	1934	2287	28.72	36.30	85.03	103.13	1.51	1.69	4.33	4.05	13.71	13.85	79.11	91.17
10	20M30B-2	1740	1102	1836	1299	20.69	30.43	29.10	44.88	2.41	2.03	4.55	4.62	11.57	14.33	23.57	33.60
11	20M30C-1	3347	4412	4269	5809	152.06	196.63	214.20	212.19	2.13	2.09	5.28	6.58	20.23	19.96	132.52	144.06
12	20M30C-2	1293	1648	2562	2343	136.35	150.54	146.52	197.66	1.61	1.62	5.15	5.56	17.24	18.14	83.08	85.79
13	35M30A-1	676	498	1048	1018	19.64	14.93	35.87	42.88	1.64	2.13	2.94	3.34	10.38	10.04	23.13	38.56
14	35M30A-2	497	672	1052	1349	16.16	22.38	43.05	44.27	1.68	1.89	3.90	3.72	10.48	16.95	33.45	31.04
15	35M30B-1	837	1166	1695	2073	71.27	59.46	143.10	119.95	2.05	2.11	4.70	4.20	17.58	19.31	164.26	123.95
16	35M30B-2	1580	2354	2463	3096	56.63	81.47	103.08	126.09	1.95	2.02	4.22	4.77	14.40	16.46	80.24	85.40
17	35M30C-1	2539	2915	3717	3347	168.92	225.51	179.72	259.18	1.61	2.45	7.13	5.55	18.44	17.34	149.45	182.21
18	35M30C-2	2597	2745	3881	3040	75.40	141.10	97.60	155.20	1.79	2.32	5.77	6.55	18.06	22.24	101.30	103.90

* CH1 = data from sensor 1 and CH2 = data from sensor 2

3.4. Damage Quantification Using AE Intensity Analysis

As previously noted, the AE intensity analysis parameters (*H (t)* and S_r) were sensitive to the successive degrees of degradation due to loss of bond in the tested pull-out specimens. These parameters have been exploited in a number of previous studies to represent different damage mechanisms in concrete structures (Nair and Cai, 2010; Abdelrahman et al., 2015; ElBatanouny et al., 2014). The results of *H (t)* and S_r at the stages of micro-cracking and macro-cracking demonstrated in **Table 5** were utilized to create a damage classification chart (**Fig. 4)**. This chart uses the relationship between *H (t)* and S_r readings to indicate the micro-cracking stage of bond stresses. If the values of *H (t)* and S_r range between 1.51–2.45 and 5.52–22.20 x 10^4 pV.s, respectively, micro-cracking of concrete is expected to be present at the steel-concrete interface. Beyond *H (t)* and S_r readings of 2.45 and 22.20 x 10^4 pV.s, respectively, macro-cracking in the

surrounding concrete core around the steel bar is anticipated. It can be noticed from the chart that the magnitudes of *H (t)* and S_r at the stage of macro-cracking showed a wide range of increase following the micro-cracking region. The ranges for this macro-cracking stage were 2.45–7.13 for *H (t)* and 22.20–182.21 x 10^4 pV.s for S_r. These wide ranges were attributed to the large differences in the sizes of splitting cracks and the significant impact of using variable bar diameter and embedded length on the AE intensity analysis parameters. However, this chart may be especially beneficial for early detection of bond deterioration between concrete and steel at the micro-cracking stage. At this stage, no visible signs of cracking or bar slippage were detected in all tested samples.

Moreover, the evaluation of *H (t)* results enabled the differentiation between samples failed by bar yield from those subjected to bond splitting failure. For example, an average *H (t)* value of 0.84 was obtained from the samples that exhibited bar yield with no damage in the bond integrity (**Table 5**). This average value corresponds to the maximum load recorded right before the bar yield (**Table 3**). These observations illustrate the accuracy of the *H (t)* in both detecting the onset of micro-cracking and representing mode of failure among the tested specimens. It is worth noting that further verification of the results in this chart are needed to generalize those parameters based on testing full-scale reinforced concrete elements.

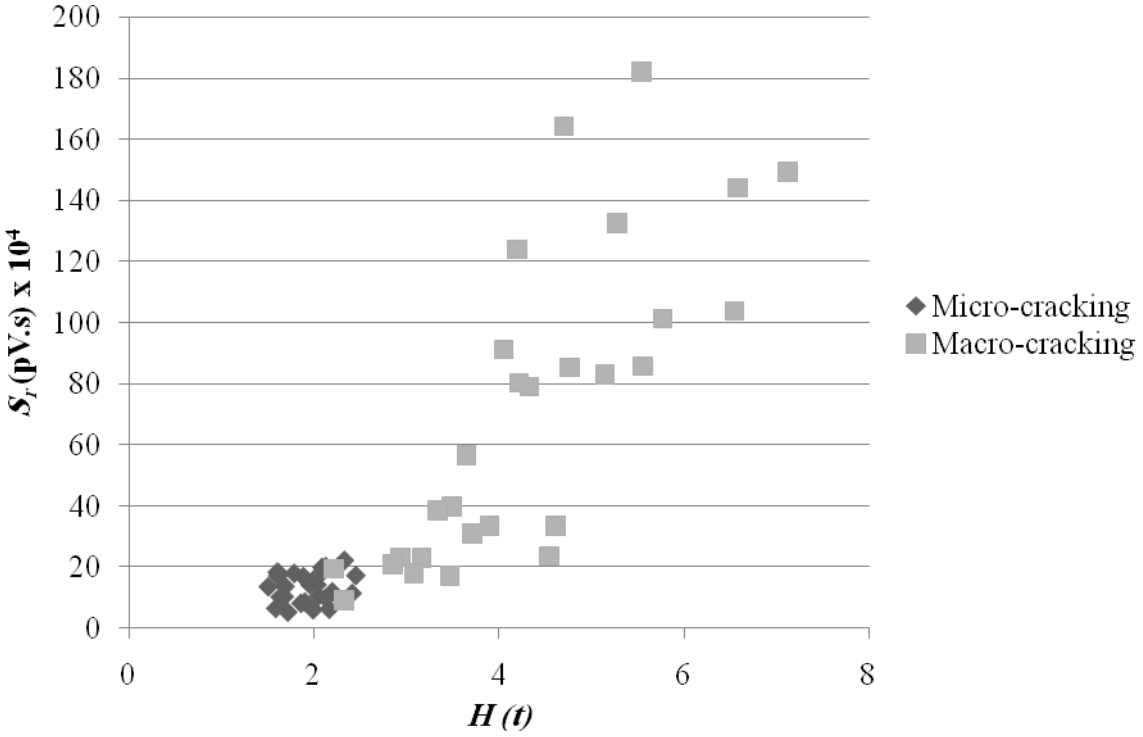

Fig. 4 Micro-cracking and macro-cracking damage classification chart

4. Conclusions

This experimental investigation utilized acoustic emission monitoring to evaluate the steel-concrete bond integrity. A total of 18 small-scale reinforced concrete prism samples were examined in pull-out tests, while being monitored by AE sensors. The variables included bar diameter (10, 20, and 35 mm) and embedded length (50, 100, and 200 mm). The AE data collected during these tests were analyzed and compared with the results of the bond behaviour of all specimens. Furthermore, an intensity analysis was completed on the AE signal strength data for the purpose of damage quantification corresponding to bond degradation. Based on the

analysis of the results and discussion presented in this article, the following conclusions were obtained:

- By reviewing the CSS versus test time curves of different tested specimens, it was possible to categorize the mode of failure and to detect two stages of bond deterioration including micro-cracking and macro-cracking. These two stages were identified at the points of slope change in the CSS curves. Accordingly, any linearity in the CSS curve indicates no bond deterioration in the tested specimen. These stages were further confirmed using intensity analysis and were pinpointed at the locations of sudden rise in the magnitudes of *H (t)* throughout the test.
- *H (t)* showed to be more numerically sensitive than all other AE parameters for early detection of the micro-cracking stage of bond damage, with values ranging from 1.51 to 2.45 in all tested samples. At this early stage, no visible cracking or bar slippage were noticed in any of the tested prism samples. In addition, the growth of splitting cracks following the micro-cracking stage were accompanied by an overall increasing trend in the results of cumulative number of hits, CSS, *H (t)*, and S_r in all tested samples.
- Intensity analysis parameters (*H (t)* and S_r) were correlated with both micro-cracking and macro-cracking stages to generate damage classification charts. Using this chart, it is possible to characterize the stage of bond deterioration (micro-cracking and macro-cracking) based on the collected AE parameters (*H (t)* and S_r).
- Further investigation into the implementation of AE monitoring for the assessment of bond behaviour of full-scale reinforced concrete elements is recommended to verify the results attained from this preliminary study.

References

Abdelrahman M, ElBatanouny MK and Ziehl PH (2014) Acoustic emission based damage assessment method for prestressed concrete structures: modified index of damage. *Engineering Structures* 60: 258–264.

Abdelrahman M, ElBatanouny MK, Ziehl P, Fasl J, Larosche CJ and Fraczek J (2015) Classification of alkali–silica reaction damage using acoustic emission: A proof-of-concept study. *Construction and Building Materials* 95: 406–413.

ACI Committee 408 (2003) Bond and development of straight reinforcing bars in tension. ACI 408R-03, American Concrete Institute, Farmington Hills, Michigan, 49 pp.

ASTM (2011) Standard test method for splitting tensile strength of cylindrical concrete specimens. ASTM C496. ASTM International: West Conshohocken, PA.

ASTM (2012a) Standard specification for portland cement. ASTM C150. ASTM International: West Conshohocken, PA.

ASTM (2012b) Standard test method for compressive strength of cylindrical concrete specimens. ASTM C39. ASTM International: West Conshohocken, PA.

ASTM (2014) Standard terminology for nondestructive examinations. ASTM E1316. ASTM International: West Conshohocken, PA.

CEB-FIP (2000) State-of-the-art report on bond of reinforcement in concrete. State-of-Art Report Prepared by Task Group Bond Models (former CEB Task Group 2.5) FIB -Féd. Int. du Béton 1–97.

ElBatanouny MK, Mangual J, Ziehl PH and Matta F (2014) Early corrosion detection in prestressed concrete girders using acoustic emission. *Journal of Materials in Civil Engineering* 26: 504–511.

Fowler T, Blessing J and Conlisk P (1989) New directions in testing. In: Proceedings, Int. Conf. of Acoustic Emission from Composite Materials, K. Ono, ed., Acoustic Emission Working Group, Memphis, TN, 16–27.

Gallego A, Benavent-Climent A and Suarez E (2015) Concrete-galvanized steel pull-out bond assessed by acoustic emission. *Journal of Materials in Civil Engineering.* Epub ahead of print 16 July 2015. DOI: 10.1061/(ASCE)MT.1943-5533.0001372, 04015109.

Grosse CU, Reinhardt HW and Finck F (2003) Signal-based acoustic emission techniques in civil engineering. *Journal of Materials in Civil Engineering* 15(3): 274–279.

Ho SCM, Ren L, Labib E, Kapadia A, Mo Y-L, Li H, Song G (2015) Inference of bond slip in prestressed tendons in concrete bridge girders. *Structural Control and Health Monitoring* 22: 289–300.

Iwaki K, Makishima O, Tanaka H, Shiotani T and Ozawa K (2003) Evaluation of bond behavior of reinforcing bars in concrete structures by acoustic emission. *Journal of Acoustic Emission* 21:166–175.

Mangual J, ElBatanouny M, Ziehl P and Matta F (2013a) Acoustic-emission-based characterization of corrosion damage in cracked concrete with prestressing strand. *ACI Materials Journal* 110(1): 89–98.

Mangual J, ElBatanouny M, Ziehl P and Matta F (2013b) Corrosion damage quantification of prestressing strands using acoustic emission. *Journal of Materials in Civil Engineering* 25(9): 1326–1334.

Mistras Group (2007) PCI-2 based AE system 1 user's manual. Physical Acoustics Corporation, Princeton Junction, NJ, USA.

Nair A and Cai CS (2010). Acoustic emission monitoring of bridges: review and case studies. *Engineering Structures* 32(6): 1704–1714.

Nilson A, Darwin D and Dolan CW (2004) *Design of concrete structures*. New York: McGraw-Hill.

Physical Acoustics (2005) R6I-AST sensor. Princeton Junction, NJ, USA.

Pollock AA (1986) Classical wave theory in practical AE testing. In: Proceedings, *Int. Acoustic Emission Symp.*, Japanese Society for Nondestructive Testing, 708–721.

Rizzo P, Spada A, Degala S and Giambanco G (2010) Acoustic emission monitoring of chemically bonded anchors. *Journal of Nondestructive Evaluation* 29: 49–61.

Vélez W, Matta F and Ziehl P (2015) Acoustic emission monitoring of early corrosion in prestressed concrete piles. *Structural Control and Health Monitoring* 22: 873–887.

Zhu XQ, Hao H and Fan KQ (2013) Detection of delamination between steel bars and concrete using embedded piezoelectric actuators/sensors. *Journal of Civil Structural Health Monitoring* 3: 105–115.

Ziehl P (2008) Applications of acoustic emission evaluation for civil infrastructure. In: Proceedings, *Smart Structures and Materials, Nondestructive Evaluation and Health Monitoring*, Society of Photo-Optical Instrumentation Engineers, Bellingham, WA, 693401.